



Fabrication of ternary g-C₃N₄/Al₂O₃/ZnO heterojunctions based on cascade electron transfer toward molecular oxygen activation

Shao-jia Liu^a, Fa-tang Li^{a,*}, Yi-lei Li^a, Ying-juan Hao^a, Xiao-jing Wang^a, Bo Li^b, Rui-hong Liu^a

^a College of Science, Hebei University of Science and Technology, Shijiazhuang, China

^b Analytical & Testing Center of Hebei Province, Hebei University of Science and Technology, Shijiazhuang, China



ARTICLE INFO

Article history:

Received 22 February 2017

Received in revised form 15 April 2017

Accepted 25 April 2017

Available online 27 April 2017

Keywords:

g-C₃N₄

Amorphous Al₂O₃

Heterojunction

Cascade electron transfer

Lattice matching

ABSTRACT

The mismatches of lattices and energy bands in heterojunction are the dominant factors restricting the generation efficiency of reactive oxygen species (ROS) that are powerful tools for water purification and anti-bacteria. In this paper, the mediated lattice matching role of amorphous Al₂O₃ is presented for constructing the ternary g-C₃N₄/Al₂O₃/ZnO heterojunctions, which exhibit higher molecular oxygen activation performance than binary g-C₃N₄/ZnO and g-C₃N₄/Al₂O₃ heterojunctions. The oxygen activation ability and the ROS generation were testified by the electron paramagnetic resonance (EPR) measurement, transformation of nitroblue tetrazolium (NBT) and degradation of methylene blue (MB). The ROS include superoxide anion radical ($\bullet\text{O}_2^-$) and consequent product of hydroxyl radical ($\bullet\text{OH}$). The superior oxygen activation performance of the ternary heterojunctions can be attributed to the lattices matching of the mediated amorphous Al₂O₃ and the resultant efficient cascade electron transfer.

© 2017 Elsevier B.V. All rights reserved.

1. Introduction

Molecular oxygen (O₂) existed in the atmosphere is the most economical and green potential oxidant. Unfortunately, it is hard to oxidize organic substances under ambient conditions by employing O₂ directly because of its spin forbidden character [1,2]. Therefore, activating molecular oxygen to generate reactive oxygen species (ROS), typically including both free radicals (superoxide anion radical, $\bullet\text{O}_2^-$; hydroxyl radical, $\bullet\text{OH}$) and non-radical forms (singlet oxygen, $^1\text{O}_2$; hydrogen peroxide, H₂O₂) [3,4], is an effective strategy to initiate the desired oxidation reactions, such as CO oxidation [5,6], alcohol oxidation [7,8], and degradation of toxic pollutants [2,9,10]. Generally, noble metal nanoparticles including Au, Ag, Pd, Pt are needed to activate O₂ [5–7,10,11], which is an expensive process and thus would reduce the strength of O₂ as a cheap oxidant.

Semiconductor photocatalysis is another feasible technique and has drawn increasing attention because of its high efficiency, low cost, and mild operation, which can allow the production of $\bullet\text{O}_2^-$ via one-electron reduction of O₂ and consequently the generation

of $\bullet\text{OH}$, or the formation of H₂O₂ through two-electron reduction of O₂ upon light irradiation [2,8,9,12]. To achieve the aim of O₂ activation, the potential of semiconductor conduction band (CB) should be more negative than –0.28 V versus standard hydrogen electrode (SHE) in solution of pH = 7 because –0.28 V is the redox potential of O₂/ $\bullet\text{O}_2^-$ that can reduce and activate O₂ to generate $\bullet\text{O}_2^-$ [13]. This requirement of potential limits the application of some photocatalysts in O₂ activation.

g-C₃N₄ has received extensive attention due to its attracting electronic band structure, high physicochemical stability, nontoxic, and “earth-abundant” nature [14,15] since Wang et al. reported its photocatalytic ability in H₂ evolution [16]. Importantly, the lowest unoccupied molecular orbital (LUMO) position of g-C₃N₄ is –1.13 V [17], which makes g-C₃N₄ to be an ideal candidate for activating O₂. Nevertheless, pristine g-C₃N₄ usually exhibit low quantum efficiency because of its relatively fast recombination of photo-induced electrons and holes [18]. Some strategies including noble metal deposition [19,20], ion modification [21], and nanoarchitecture [15] design have been employed for improving its photocatalytic activity. Building heterojunctions is another effective method through which photo-induced electrons on LUMO of g-C₃N₄ can migrate to the CB of other semiconductors [22,23]. It should be noted that two factors are crucial in constructing hetero-

* Corresponding author.

E-mail address: lifatang@126.com (F.-t. Li).

junctions for oxygen activation: one is the energy bands matching capable of transferring electrons from $\text{g-C}_3\text{N}_4$ to the other component. From this point of view, TiO_2 or ZnO whose conduction bands are above -0.28 V can be selected to be combined with $\text{g-C}_3\text{N}_4$ [24]. The other factor is the lattice matching degree of the two semiconductors, which has great influence on charge transfer and separation at the heterojunction interfaces [25,26]. However, it is difficult to reach the lattice matching between $\text{g-C}_3\text{N}_4$ and metal oxides because of their different crystal structures and lattice parameters, such as $\text{g-C}_3\text{N}_4$ and ZnO [27]. Hence, seeking for appropriate mediated materials as a bridge to connect $\text{g-C}_3\text{N}_4$ and metal oxides for fabricating ternary heterojunctions should be a feasible strategy.

Amorphous materials have characteristics of disordered atomic distribution and unfixed lattice parameters, which would endow them more convenient charge acceptance performance from $\text{g-C}_3\text{N}_4$ than crystals. Our group previous studies verified that amorphous Al_2O_3 possess lots of defects, which can accept photo-induced electrons from the LUMO of $\text{g-C}_3\text{N}_4$ [18,28–30]. However, Al_2O_3 -based ternary heterostructured photocatalysts have not been reported to date.

In this case, we employed amorphous Al_2O_3 to remedy the lattice mismatch of $\text{g-C}_3\text{N}_4$ and ZnO . The role of amorphous materials in lattice match and the CB position of amorphous Al_2O_3 obtained via precipitation are presented for the first time. The as-prepared ternary $\text{g-C}_3\text{N}_4\text{-Al}_2\text{O}_3\text{-ZnO}$ heterojunctions exhibit superior molecular oxygen activation performance via cascade electron transfer route, which is evaluated by the electron paramagnetic resonance (EPR) measurement, transformation of nitroblue tetrazolium (NBT) and degradation of methylene blue (MB). In this case, all the components of $\text{g-C}_3\text{N}_4$, ZnO , and Al_2O_3 are earth-abundant, which makes ternary $\text{g-C}_3\text{N}_4\text{-Al}_2\text{O}_3\text{-ZnO}$ to be an ideal inexpensive photocatalyst candidate. This work would broaden the application of amorphous materials in preparing heterojunctions and provide references for the development of inexpensive photocatalysts and the design route of molecular oxygen activation.

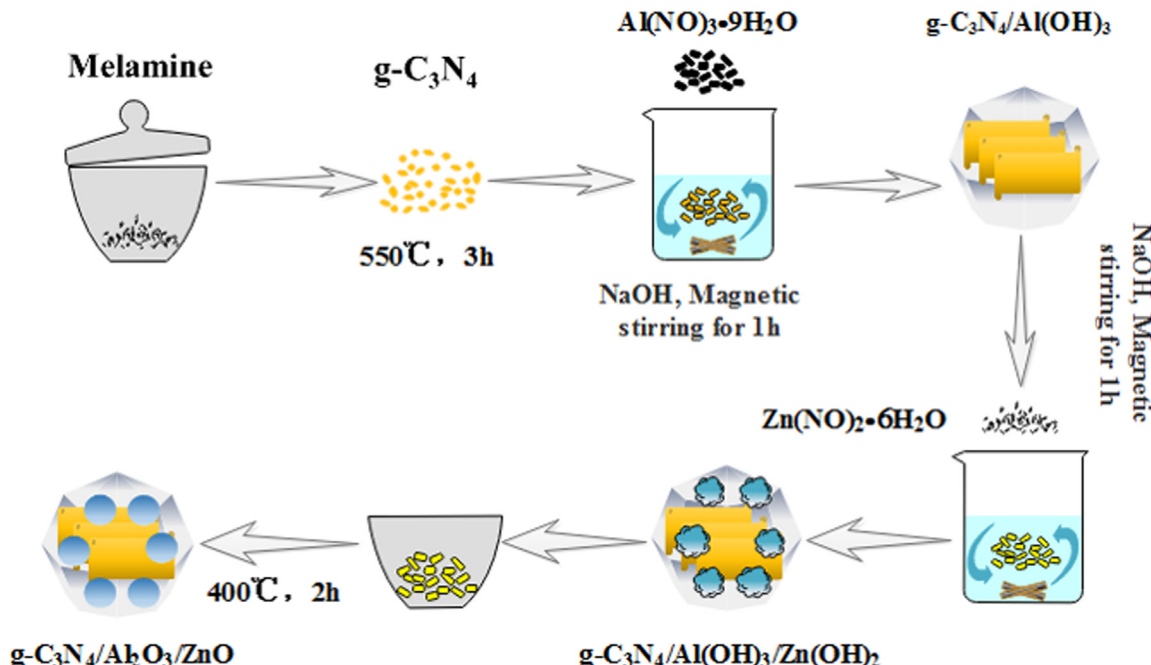
2. Experimental section

2.1. Materials and samples synthesis

$\text{Al}(\text{NO}_3)_3\cdot 9\text{H}_2\text{O}$, $\text{Zn}(\text{NO}_3)_2\cdot 6\text{H}_2\text{O}$ and NaOH were obtained from Aladdin Reagents Co. Ltd (Shanghai, China). Melamine, Na_2SO_4 , methylene blue (MB), ammonium oxalate monohydrate (AO), 1,4-benzoquinone (BQ), isopropanol ($i\text{-PrOH}$), terephthalic acid (TA), nitrotetrazolium blue chloride (NBT) were purchased from Sinopharm Chemical Reagent Co. Ltd (Shanghai, China). All the reagents were of analytical grade and used without further purification.

Pure $\text{g-C}_3\text{N}_4$ powders were prepared by directly calcining melamine in a muffle furnace according to Ref. [16]. As a classic experiment step, 5 g of melamine was placed in an alumina crucible. The crucible was semi-covered and heated to 550°C for 3 h at a heating rate of $20^\circ\text{C}/\text{min}$. After cooling to room temperature, yellow $\text{g-C}_3\text{N}_4$ was obtained in a powder form.

The ternary $\text{g-C}_3\text{N}_4/\text{Al}_2\text{O}_3/\text{ZnO}$ heterojunctions were synthesized via the hydrothermal and calcination process. Typically, the synthesis procedure of ternary 50%wt $\text{g-C}_3\text{N}_4$ /40%wt Al_2O_3 /10%wt ZnO (abbreviated as 50C/40A/10Z) was conducted as follows: firstly, 1.765 g $\text{Al}(\text{NO}_3)_3\cdot 9\text{H}_2\text{O}$ was dissolved in 40 mL of distilled water and then mixed with 0.3 g $\text{g-C}_3\text{N}_4$ under continuous stirring. Secondly, 1 mol/L NaOH solution was added dropwise to the mixture till the pH at around 9. After 1 h stirring, 0.220 g $\text{Zn}(\text{NO}_3)_2\cdot 6\text{H}_2\text{O}$ was added into the disperse system and 1 mol/L NaOH solution was added to keep the solution pH at ca. 9. After stirring this mixture for another 1 h, yellow precipitate powders were filtered and washed with distilled water for five times. Thirdly, after being dried at 110°C for 2 h, the resultant solid powders were calcined at 400°C for 2 h with a heating rate of $5^\circ\text{C}/\text{min}$. Finally, the sample was taken out and ground. This process is illustrated as shown in Scheme 1. By varying the amount of $\text{Al}(\text{NO}_3)_3\cdot 9\text{H}_2\text{O}$ and $\text{Zn}(\text{NO}_3)_2\cdot 6\text{H}_2\text{O}$, various ternary heterojunctions could be obtained and were labeled as XC/YA/MZ (X, Y, M represent the corresponding weight content of $\text{g-C}_3\text{N}_4$, Al_2O_3 , and ZnO). Binary 50C/50A and 50C/50Z were syn-



Scheme 1. Schematic illustration for the preparation of $\text{g-C}_3\text{N}_4\text{/Al}_2\text{O}_3\text{/ZnO}$ ternary heterojunction.

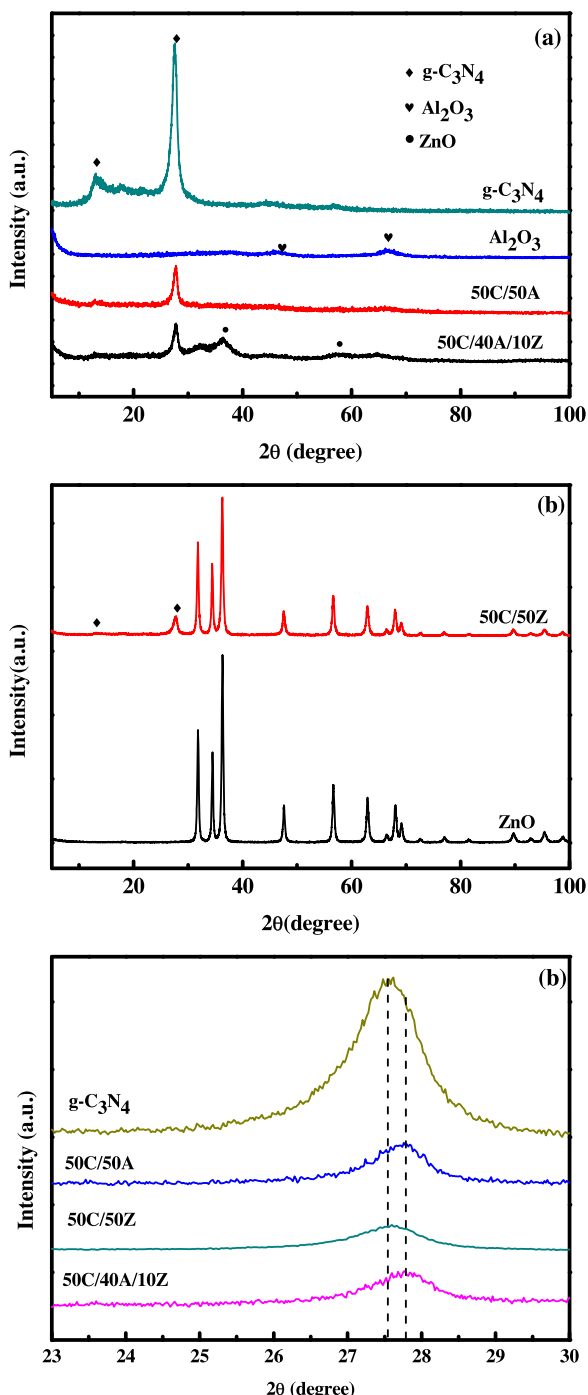


Fig 1. (a) XRD patterns of pure g-C₃N₄, Al₂O₃, ZnO and various heterojunctions; (b) magnified peaks of g-C₃N₄ and heterojunctions.

thesized without the addition of Zn(NO₃)₂·6H₂O or Al(NO₃)₃·9H₂O, respectively.

2.2. Materials characterization

The powder X-ray diffraction (XRD) patterns were obtained from an XRD diffractometer (Rigaku D/max-2500) using Cu K α radiation in the range of 10–100° at a scan rate of 0.02° min⁻¹. Nitrogen sorption analysis was performed using a porosity analyser (Micromeritics Tristar II 3020 apparatus). The surface areas were calculated using the Brunauer–Emmett–Teller (BET) method. Pore size distribution including pore diameter and pore volume

was obtained using Barrett–Joyner–Halenda (BJH) approach. The morphology was observed by using a JEOL JEM-2010 microscope transmission electron microscope (TEM). The X-ray photoelectron spectroscopy (XPS) experiment was performed on a PHI 1600 ESCA X-ray photoelectron spectrometer with a monochromatic source Al K α to investigate the chemical states of elements. Furthermore, optical properties were analyzed by acquiring diffuse reflectance spectra (DRS) using a UV-vis spectrophotometer (Thermo Scientific Evolution 220 spectrophotometer) in the range of 200–800 nm. Time-resolved photoluminescence (PL) studies were conducted using a fluorescence spectrophotometer (FS5, Edinburgh Instruments) with an ultraviolet exciter at excitation wavelength (λ_{ex}) of 254 nm as the excitation light source. Photoelectrochemical measurements were carried out on an electrochemical workstation (CHI-660E, China) by using a conventional three-electrode quartz cells. An aqueous solution containing 0.2 M Na₂SO₄ was employed as electrolyte. The counter and reference electrodes were platinum wire and Ag/AgCl, respectively. The as-obtained photocatalyst film electrodes deposited on cleaned 1.5 cm × 1.0 cm fluoride-tin oxide (FTO) glass served as the working electrode.

2.3. Evaluation of molecular oxygen activation

To compare the generation and amount of active oxygen species, electron paramagnetic resonance (EPR) signals of radicals spin-trapped by 5,5-dimethyl-L-pyrroline-N-oxide (DMPO) were collected on a Bruker EMX-8/2.7 X-band EPR spectrometer under visible light irradiation ($\lambda > 400$ nm). NBT (2.5×10^{-5} mol/L) was employed as an indicator of •O₂⁻ because NBT exhibits a maximum absorption at 259 nm, while the product of NBT and •O₂⁻ does not [31,32]. To detect whether there are •OH radicals, the 2-hydroxyterephthalic acid (TAOH) fluorescence method was taken because •OH can react with TA to form TAOH which is a high fluorescent compound [33]. To carry out TAOH tests, TA was firstly dissolved in 2.0 mM NaOH to obtain a 0.5 mM solution for the next experiment. MB (20 mg/L) was used as a model pollutant to further evaluate the photocatalytic activity of all the prepared samples. To perform the photocatalytic experiments, 300 W xenon lamp with a $\lambda > 420$ nm cut-off filter was employed as visible-light source. Then, 100 mL of NBT, TA, or MB solution was added in a beaker and mixed with 0.1 g of the photocatalyst. Then the mixture was stirred in the dark for 60 min to attain adsorption/desorption equilibrium, and the solution began to be illuminated under light. A 5 mL suspension was taken out at 10 min intervals and centrifuged at 6000 rpm for 10 min to remove the photocatalyst powders. The concentrations of NBT and MB were analyzed by UV-vis spectrophotometer (Thermo Scientific Evolution 220 spectrophotometer) at the maximum absorption wavelength (259 nm for NBT and varying wavelength for MB). The production of H₂O₂ was determined by another fluorescence route by employing *p*-hydrophenylacetic acid (POPHA), which can be oxidized to a fluorescence product 5,5'-dicarboxymethyl-2,2-dihydroxybiphenyl by a peroxidase-catalyzed reaction. The detailed experimental procedures were performed according to Ref. [12]. To evaluate the stability of the photocatalyst, the nanopowders were separated from the reaction mixture by centrifugation at 13000 r/min for 5 min and then dried at 120 °C for 2 h. The fluorescence intensity of TAOH was measured on a Hitachi F-4600 fluorescence spectrophotometer (excitation wavelength: 315 nm).

3. Result and discussion

3.1. Composition and structure of samples

After the addition of $\text{Al}(\text{NO}_3)_3 \cdot 9\text{H}_2\text{O}$ and $\text{Zn}(\text{NO}_3)_2 \cdot 6\text{H}_2\text{O}$ successively, a multi-level structured precursors were obtained. Then, ternary $\text{g-C}_3\text{N}_4/\text{Al}_2\text{O}_3/\text{ZnO}$ heterojunctions were acquired after the following calcination process. As shown in Fig. 1a, it can be seen from the pattern of $\text{g-C}_3\text{N}_4$ that there are two peaks at 13.0° and 27.5° , corresponding to (100) and (002) diffraction planes of $\text{g-C}_3\text{N}_4$ (JCPDS card No. 87-1526)[34]. Pure Al_2O_3 also has two embossment at the 46.8° and 66.7° , corresponding to (400) and (440) diffraction planes of cubic $\gamma\text{-Al}_2\text{O}_3$ (JCPDS card No. 10-0425). The broad peaks show the low crystalline degree of the Al_2O_3 and the existence of amorphous parts. From Fig. 1b, pure ZnO has nine sharp peaks, which is well consistent with hexagonal ZnO (JCPDS card No. 89-1397). The intensity peaks of $\text{g-C}_3\text{N}_4$ in the 50C/50Z composite are relatively weak compared with those of ZnO , implying the excellent crystallinity of ZnO .

As for the $\text{g-C}_3\text{N}_4/\text{Al}_2\text{O}_3$ heterojunction shown in Fig. 1a, the (002) plane peak of $\text{g-C}_3\text{N}_4$ is obvious and the peaks of Al_2O_3 can almost be not observed, indicating the main amorphous feature of Al_2O_3 . On the other hand, it can be seen from magnified pattern of Fig. 1c that there is an obvious difference from pure $\text{g-C}_3\text{N}_4$, that is, the peak at 27.5° in pure $\text{g-C}_3\text{N}_4$ shifts to 27.8° in $\text{g-C}_3\text{N}_4/\text{Al}_2\text{O}_3$ heterojunction, which implies that the intermolecular spacing of (002) plane is narrower in $\text{g-C}_3\text{N}_4/\text{Al}_2\text{O}_3$ heterojunction than that in pure $\text{g-C}_3\text{N}_4$. This result can be attributed to the coordination between the unoccupied 3p or 3d orbital of Al ion and the lone-pair electrons on N atom of $\text{g-C}_3\text{N}_4$ [18,35]. However, as shown in Fig. 1c, there is no shift at this peak in the case of $\text{g-C}_3\text{N}_4/\text{ZnO}$ heterojunction. This phenomenon means that there is no coordination effect between N atom of $\text{g-C}_3\text{N}_4$ and Zn ion of ZnO , which may be explained by that the electron configuration of Zn ion is d^{10} without unoccupied 3d orbit and the 4s vacant orbital should have no coordination effect with N atom. The diagram for coordination of Al and Zn ions with $\text{g-C}_3\text{N}_4$ are shown in Scheme 2. It is noteworthy that $\text{g-C}_3\text{N}_4/\text{Al}_2\text{O}_3/\text{ZnO}$ ternary heterojunction still occurs peak shift, indicating the close contact between $\text{g-C}_3\text{N}_4$ and Al_2O_3 .

HRTEM was further applied to confirm the formation of the ternary heterojunction. As shown in Fig. 2, the interplanar spacing of 0.17 nm corresponds to the (116) plane of $\gamma\text{-Al}_2\text{O}_3$, and that of 0.29 nm should be assigned to the (001) plane of ZnO . Meanwhile, the cotton-like parts without clear lattice fringes are attributed to amorphous or $\text{g-C}_3\text{N}_4$. Obviously, lattice fringe of ZnO intertwined with that of Al_2O_3 , together with $\text{g-C}_3\text{N}_4$ layer, can prove that they are closely linked. This compacted interfaces would provide a stair to transfer photo-induced carriers.

Fig. 3 exhibits the N_2 adsorption/desorption isotherms and the corresponding pore size distribution curves (inset) of the representative $\text{g-C}_3\text{N}_4$, binary heterojunctions and ternary 50C/40A/10Z heterojunction. The isotherms belong to IV Brunauer type with a H3 hysteresis loop [36], indicating the existence of mesoporous (2 nm–50 nm). The specific surface areas (S_{BET}), average pore diameters and total pore volumes are summarized in Table 1. The S_{BET} of pure $\text{g-C}_3\text{N}_4$ is only $14.0 \text{ m}^2/\text{g}$, while the binary heterojunction $\text{g-C}_3\text{N}_4/\text{Al}_2\text{O}_3$ or $\text{g-C}_3\text{N}_4/\text{ZnO}$ possesses bigger specific surface areas. Attractively, the surface areas of ternary heterojunctions constituted by $\text{g-C}_3\text{N}_4$, Al_2O_3 and ZnO are further increased. The high surface area would supply more active sites for the adsorption of pollutants, which is beneficial for the photocatalytic activity.

3.2. Chemical interaction analysis by XPS

To examine the interaction of various elements in heterojunctions, XPS analysis was carried out. As showed in Fig. 4a, C, N, O, Al,

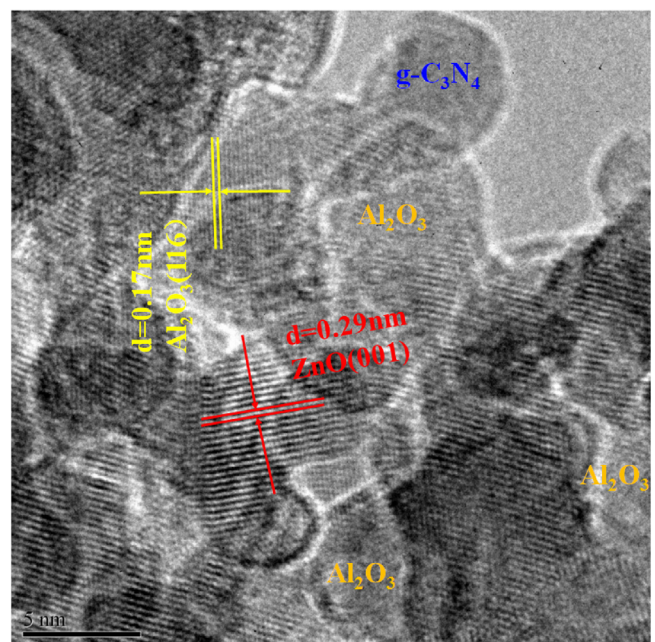


Fig. 2. HRTEM micrographs of ternary 50C/40A/10Z heterojunction.

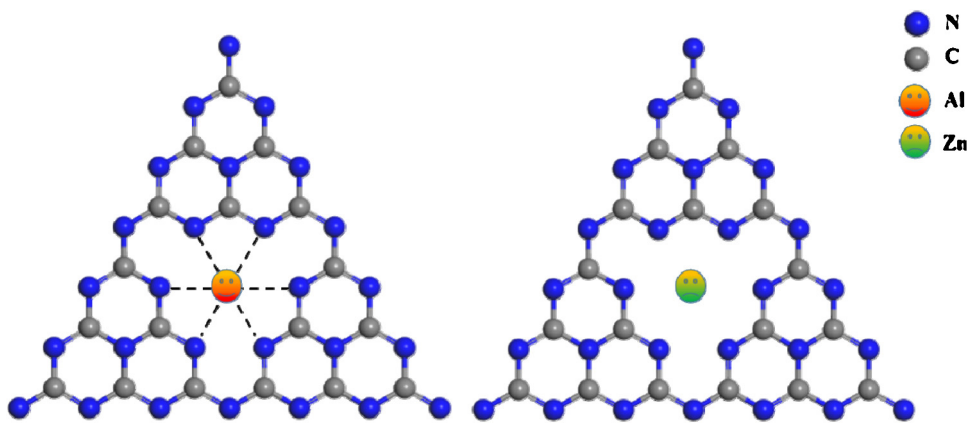
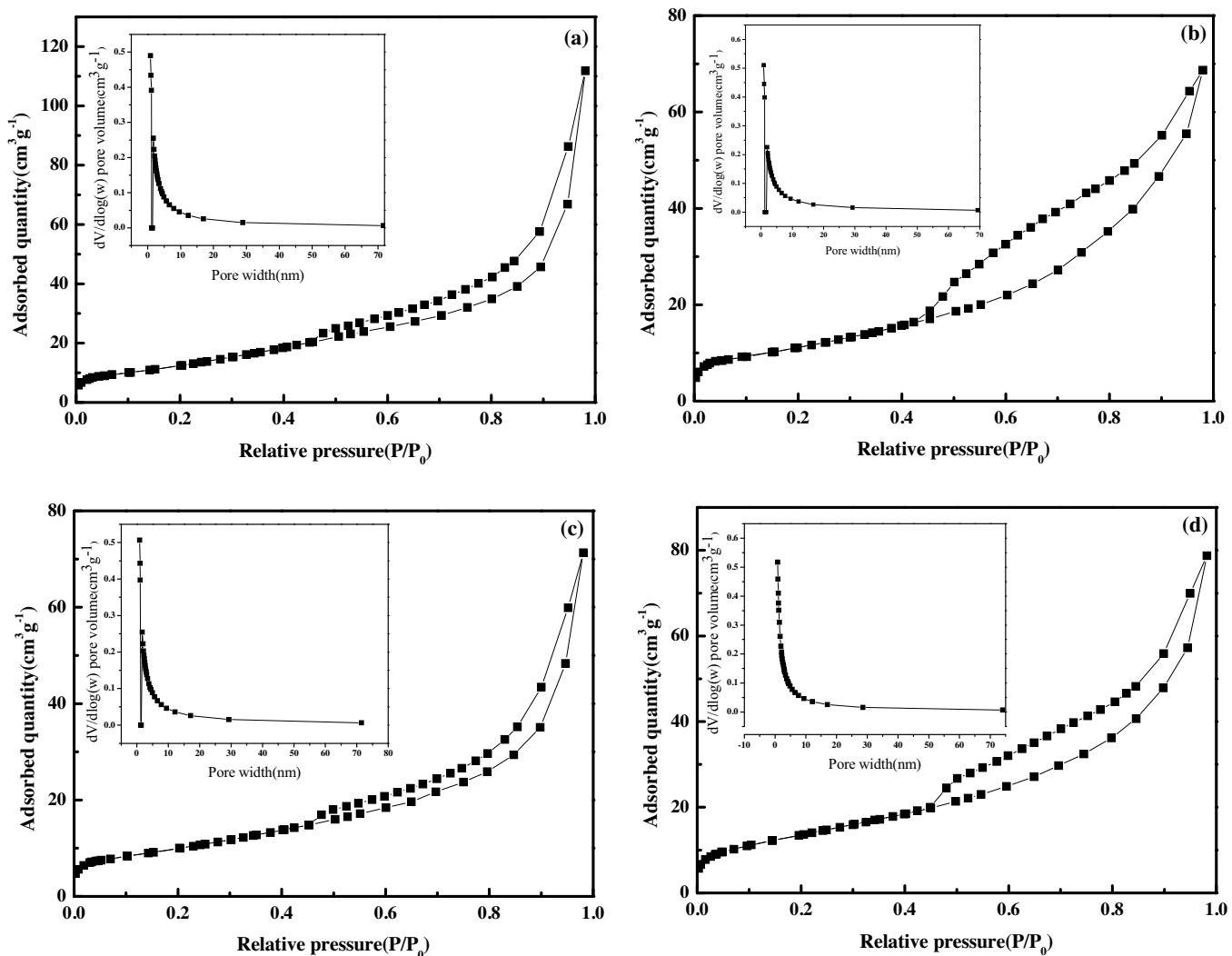
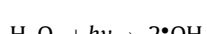
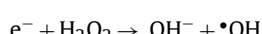
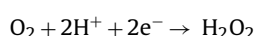
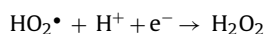
Zn can be observed in the ternary heterojunction. Fig. 4b shows the high-resolution XPS spectra of Al2p. The peak at 73.78 eV derived from pristine Al_2O_3 [37,38] shifts to a higher value of 74.08 eV or 73.88 eV in the case of 50C/50A or 50C/40A/10Z, respectively, indicating the existence of chemical interaction between Al element and $\text{g-C}_3\text{N}_4$. As for Zn element, it can be seen from Fig. 4c that the binding energies of $\text{Zn}2\text{p}3/2$ at 1020.98 eV and $\text{Zn}2\text{p}1/2$ located at 1043.9 eV of pristine ZnO [39] do not shift after the $\text{g-C}_3\text{N}_4$ combining except for the reduction of the peak intensities, showing there should be no chemical force between Zn and $\text{g-C}_3\text{N}_4$. This result is consistent with XRD, further supporting the coordination point on the difference of Al and Zn with $\text{g-C}_3\text{N}_4$.

The high-resolution XPS spectrum of N1s for $\text{g-C}_3\text{N}_4$ shown in Fig. 4d has two clear peaks at 398.35 eV and 400.30 eV, which can be ascribed to sp^2 -hybridized nitrogen atoms involved in triazine ($\text{C}=\text{N}-\text{C}$) units and amino groups ($\text{C}-\text{N}-\text{H}$), respectively [40]. In the XPS spectrum of N1s in $\text{g-C}_3\text{N}_4/\text{ZnO}$ heterojunction shown in Fig. 4e, the main peak is slightly moved to a higher value 398.44 eV from 398.35 eV, illustrating the weak connection between $\text{g-C}_3\text{N}_4$ and ZnO . While in the case of $\text{g-C}_3\text{N}_4/\text{Al}_2\text{O}_3$, the main peak is centered at 398.13 eV, showing the stronger Al-N interaction due to the coordination effect, which is also confirmed in the ternary $\text{g-C}_3\text{N}_4/\text{Al}_2\text{O}_3/\text{ZnO}$ composite in Fig. 4g. In addition, it is also can be seen from the spectra of Al2p and Zn2p shown in Fig. 4b and c, there are little shift after combining ZnO , which imply there is chemical interaction between Al_2O_3 and ZnO to some extent. All of these XPS results indicate that the $\text{g-C}_3\text{N}_4/\text{Al}_2\text{O}_3/\text{ZnO}$ heterojunction closely connected and confirm the lattice matching effect of Al_2O_3 .

3.3. Molecular oxygen activation and photocatalytic degradation performances

Following the successful synthesis of ternary heterojunctions, we investigated their performance in O_2 activation. It is known that O_2 can be activated to form reactive oxygen species mainly including $\bullet\text{O}_2^-$, H_2O_2 , and $\bullet\text{OH}$ in the photocatalytic process according to the following equations [12,41]:



**Scheme 2.** Diagrammatic sketches for the coordination effect of Al and Zn ions with N atoms of $\text{g-C}_3\text{N}_4$.**Fig. 3.** N_2 adsorption/desorption isotherms and pore size distribution curves (inset) of representative (a) $\text{g-C}_3\text{N}_4$, (b) 50C/50Z, (c) 50C/50A, and (d) 50C/40A/10Z.

Firstly, to detect the generation rate of the $\bullet\text{O}_2^-$, the transformation percentage of NBT as the transparent molecular probe was conducted. Fig. 5a shows the $(\text{C}_0 - \text{C})/\text{C}_0$ of NBT vs reaction time over pure $\text{g-C}_3\text{N}_4$, binary 50C/50A, 50C/50Z, and ternary heterojunctions with different mass ratio, where C_0 and C represents the initial concentration and concentration at time t , respectively. It is seen that $\text{g-C}_3\text{N}_4$ shows the lowest NBT transformation rate

Table 1

S_{BET} and pore parameters of samples and their photocatalytic performances for MB removal.

Sample	S_{BET} (m^2/g)	Average pore diameter (nm)	Pore volume (cm^3/g)	Fitted equation	k (min^{-1})	Correlation coefficient (R)
g-C ₃ N ₄	14.0	7.8	0.04	y = 0.0147x + 0.1255	0.0147	0.9936
50C/50A	42.2	10.1	0.11	y = 0.0148x + 0.1841	0.0148	0.9912
50C/50Z	37.5	11.8	0.11	y = 0.0119x + 0.2143	0.0119	0.9975
50C/45A/5Z	48.7	9.5	0.11	y = 0.0183x + 0.0830	0.0183	0.9950
50C/40Al/10Z	50.0	9.7	0.12	y = 0.0243x + 0.2476	0.0243	0.9968
50C/35A/15Z	46.5	9.9	0.12	y = 0.0155x + 0.0756	0.0155	0.9938
50C/30A/20Z	43.2	10.2	0.11	y = 0.0087x + 0.0069	0.0087	0.9985

due to the relatively fast combination efficiency of photo-induced electrons and holes. In binary and ternary heterojunctions, the 50C/40A/10Z shows the highest degradation rate for NBT. The phenomenon demonstrates that the production rates of $\bullet\text{O}_2^-$ radicals over 50C/40A/10Z is the fastest.

As for the production of H₂O₂, it is seen from Eqs. (2)–(4) that there are two pathways, i.e., two step single-electron reduction of O₂ or one step two-electron reduction of O₂. The H₂O₂ generation curves over g-C₃N₄ and 50C/40A/10Z are shown in Fig. 5b, from which it can be seen that the order of H₂O₂ amount is consistent with the result of $\bullet\text{O}_2^-$ radicals shown in Fig. 5a. Hence, it is speculated that the generation of H₂O₂ follows the two step single-electron reduction of O₂, not the one step two-electron reduction.

According to Eqs. (5) and (6), The produced H₂O₂ could be converted into $\bullet\text{OH}$ radicals by either photo-induced electrons or light irradiation [12,41]. $\bullet\text{OH}$ radical is also an important active oxygen species and can be measured by TAOH. The TAOH result is shown in Fig. 5c, illustrating that the peak intensity of TAOH over ternary heterojunction is increased with the irradiation time, demonstrating the existence of $\bullet\text{OH}$ radicals.

To further confirm the reactive species generated in the photocatalytic process, the degradation of MB and the scavenger experiments were performed. Fig. 6a shows the reduction in concentration of MB with respect to time using pure g-C₃N₄ and different heterojunctions. The self-degradation of MB in the absence of photocatalyst was also considered because MB is instability. It is

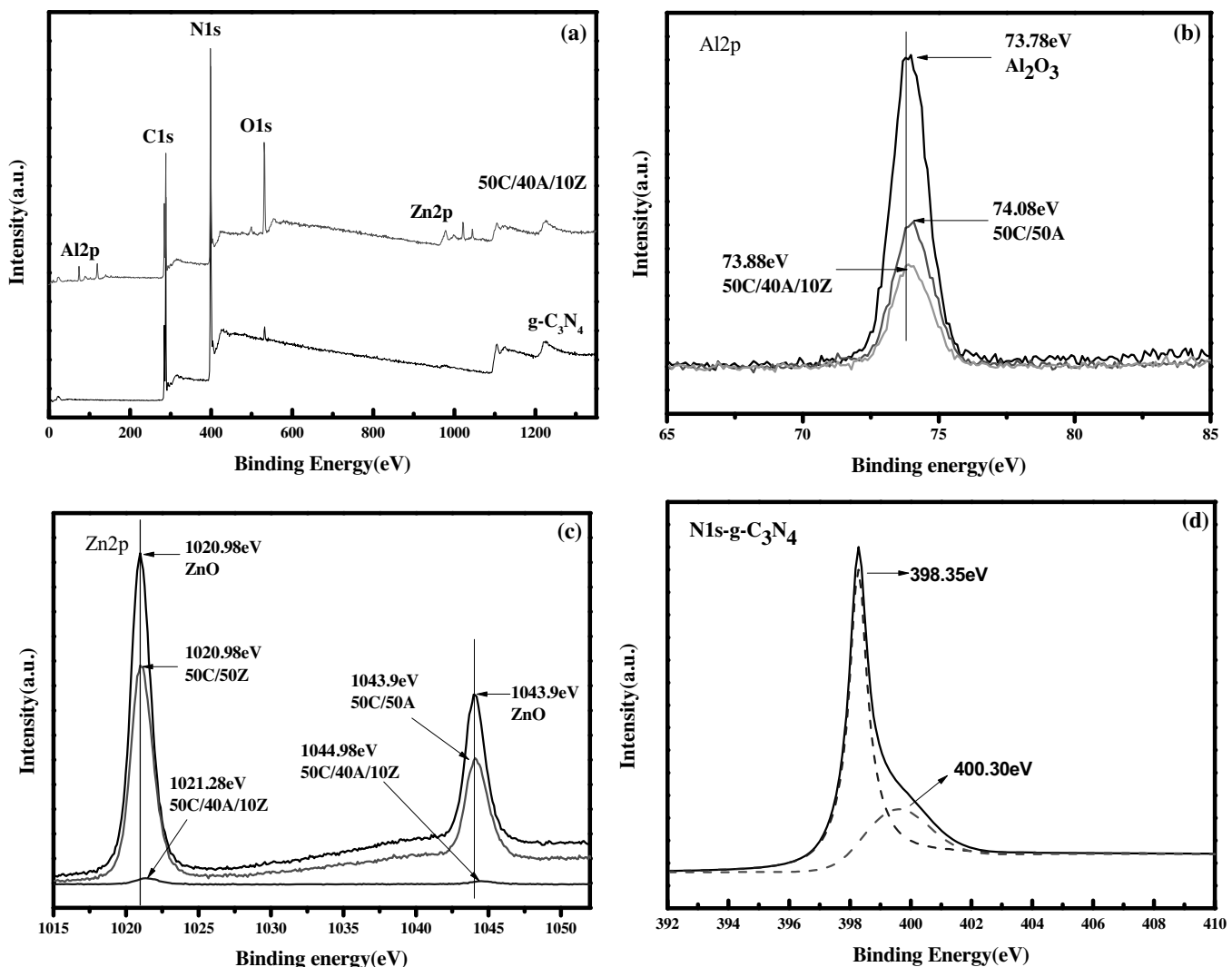


Fig. 4. (a) XPS survey spectra of bare g-C₃N₄ and ternary 50A/40A/10Z, and high resolution XPS spectra of (b) Al2p, (c) Zn2p, (d)-(g) N1 s of g-C₃N₄, 50C/50Z, 50C/50A, 50C/40A/10Z.

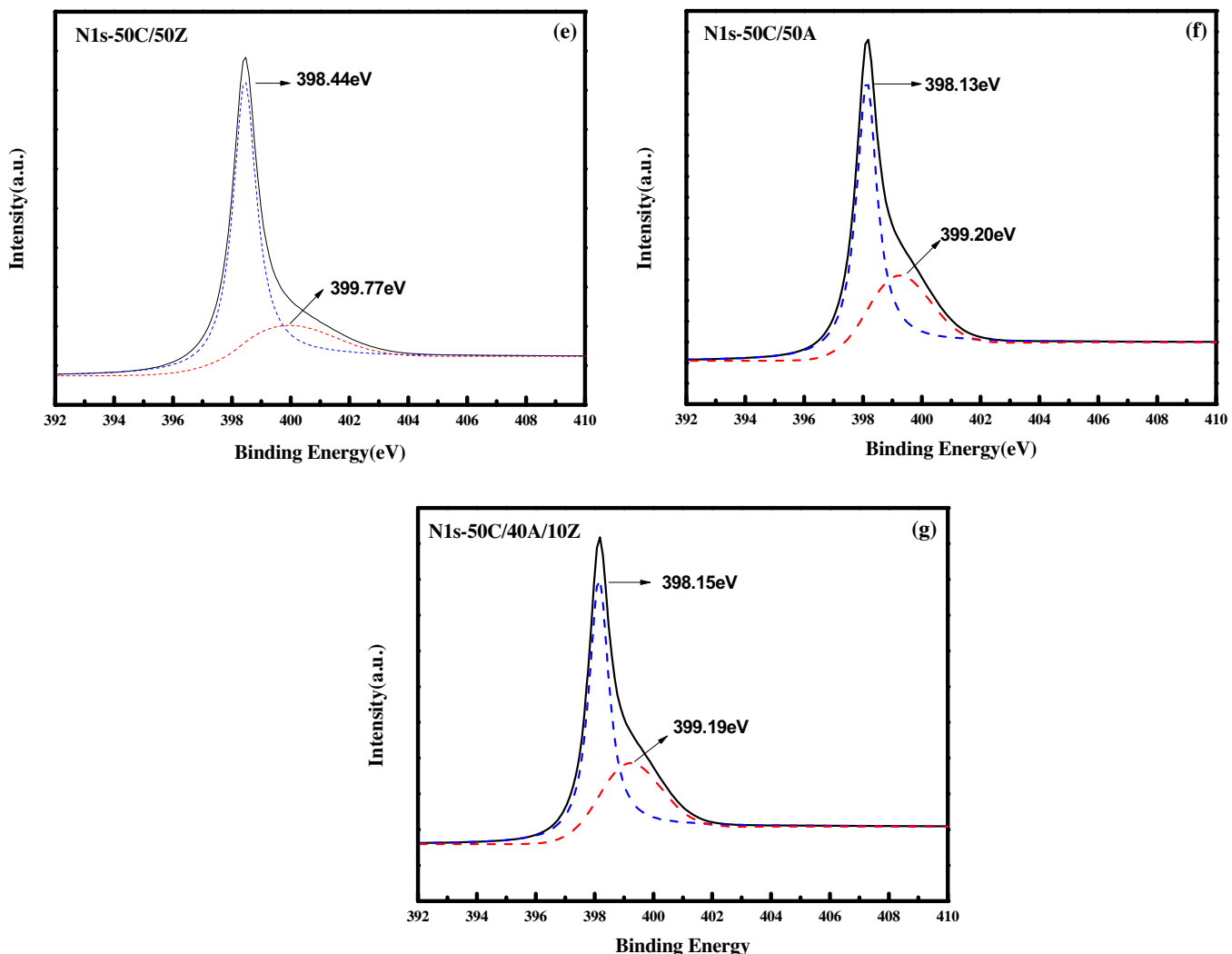


Fig. 4. (Continued)

seen that the ternary 50C/40A/10Z heterojunction shows the best photocatalytic effect with a degradation efficiency of 85% at 50 min. In order to more accurately describe the photocatalytic activity, the pseudo-first order kinetic model of the samples are determined according to the following equation [42,43]:

$$\ln(C_0/C) = kt + \ln(C_0/C_1) \quad (7)$$

where k is the reaction rate constant, C_0 is the initial concentration of MB (20 mg/L), C_1 is the concentration after 60 min adsorption, and C is the MB concentration at irradiation time t . The time-course variation of $\ln(C_0/C)$ of all the samples are illustrated in Fig. 6b. Because the value of $\ln(C_0/C_1)$ represents the adsorption efficiency of photocatalyst for pollutant molecules, the fitting curves for the plots of $\ln(C_0/C)$ are coerced to go through the intercepts of $\ln(C_0/C_1)$ in the y-axis [42]. The results of calculated intercepts, rate constants k , and correlation coefficients (R) are listed in Table 1. From Fig. 6 and Table 1, it is clear that the 50C/40A/10Z sample exhibits the highest adsorptive ability for MB with an intercept of 0.2476, which may be related to the synergistic effect of specific surface area and surface charge, and the high surface area is beneficial for the subsequent photocatalytic degradation process [20]. Meanwhile, the pure g-C₃N₄ has a relatively low rate constant of only 0.0147 min⁻¹, and the ternary 50C/40A/10Z heterojunction shows the highest rate constant of 0.0243 min⁻¹, which is 1.66 times that of pure g-C₃N₄. Compared with the O₂ activation results

shown in Fig. 5a, although g-C₃N₄/Al₂O₃ and g-C₃N₄/ZnO exhibits higher O₂ activation ability than pure g-C₃N₄ (almost 1.46 times), their photocatalytic activities are not improved in degradation of MB, indicating that •O₂⁻ is not the sole decisive factor responsible for the photocatalytic degradation of pollutants.

The stability of the 50C/40A/10Z heterojunction was demonstrated by performing three cycles of MB degradation. The results shown in Fig. 7 clearly display that the photocatalytic degradation efficiency is slight decreased after three cycles of experiment, stating that this sample is a stable photocatalyst.

3.4. Active oxygen species detection

To investigate the reactive species generated in the photocatalytic process that is responsible for the MB degradation, the scavenger experiments over 50C/40A/10Z heterojunction were carried out by employing ammonium oxalate monohydrate (AO, 2 mM) as h⁺ scavenger [44], 1,4-benzoquinone (BQ, 1 mM) as •O₂⁻ scavenger [45], and isopropanol (i-PrOH, 10 mM) as •OH scavenger [46], respectively. As shown in Fig. 8, it is seen that the addition of 1 mM BQ most acutely decreases the photodegradation yield of MB, which implies that •O₂⁻ is the dominant species accounting for the MB degradation. Meanwhile, BQ and i-PrOH can also depress the degradation of MB, indicating that •O₂⁻ and •OH are the active species at the same time. Because the position of g-C₃N₄ LUMO is

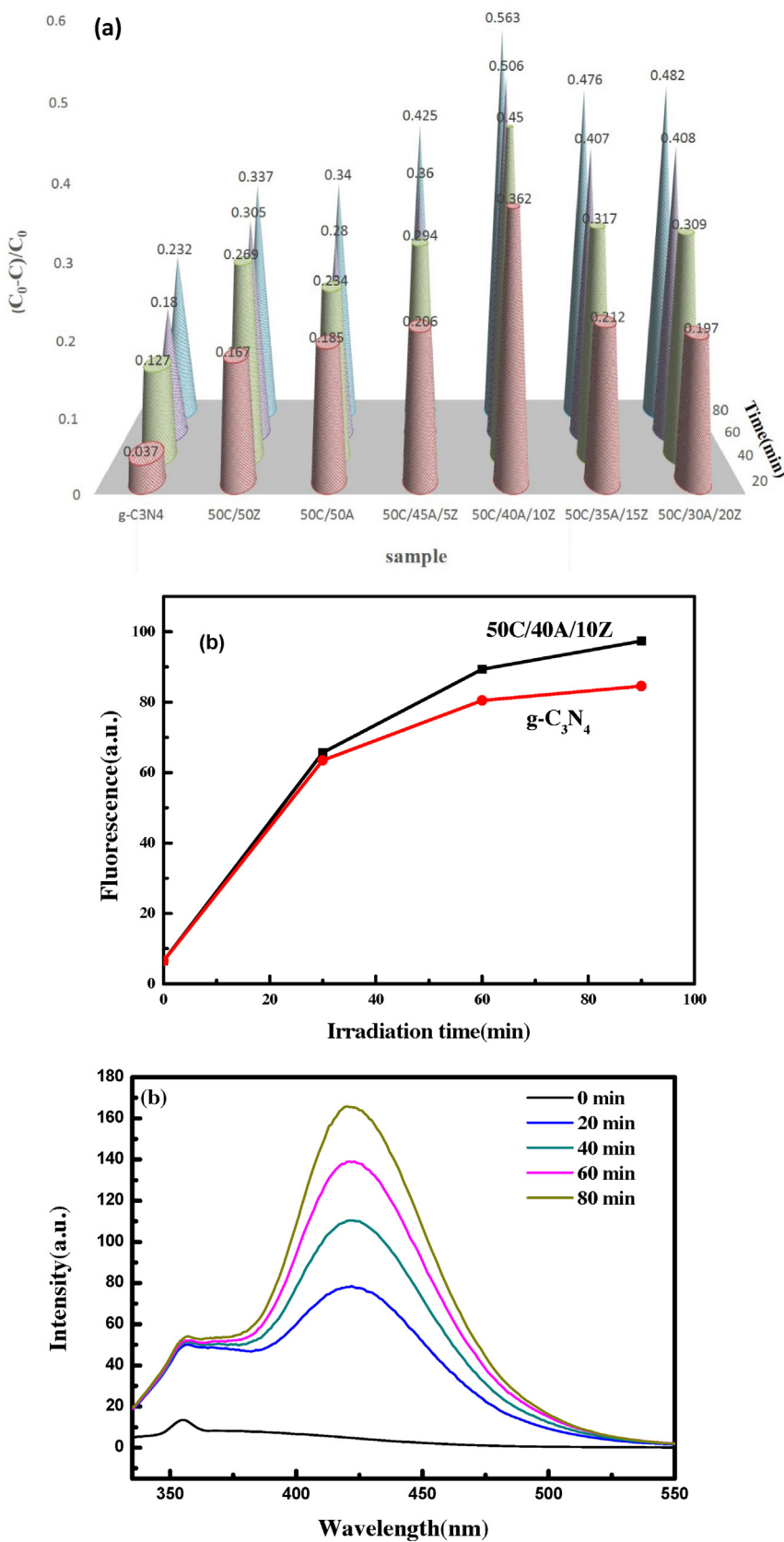


Fig. 5. (a) Transformation percentage of NBT in the time-course variation over various samples, (b) H₂O₂ generation curves over g-C₃N₄ and 50C/40A/10Z under visible light irradiation, and (c) TAOH fluorescence intensity over 50C/40A/10Z ternary heterojunction.

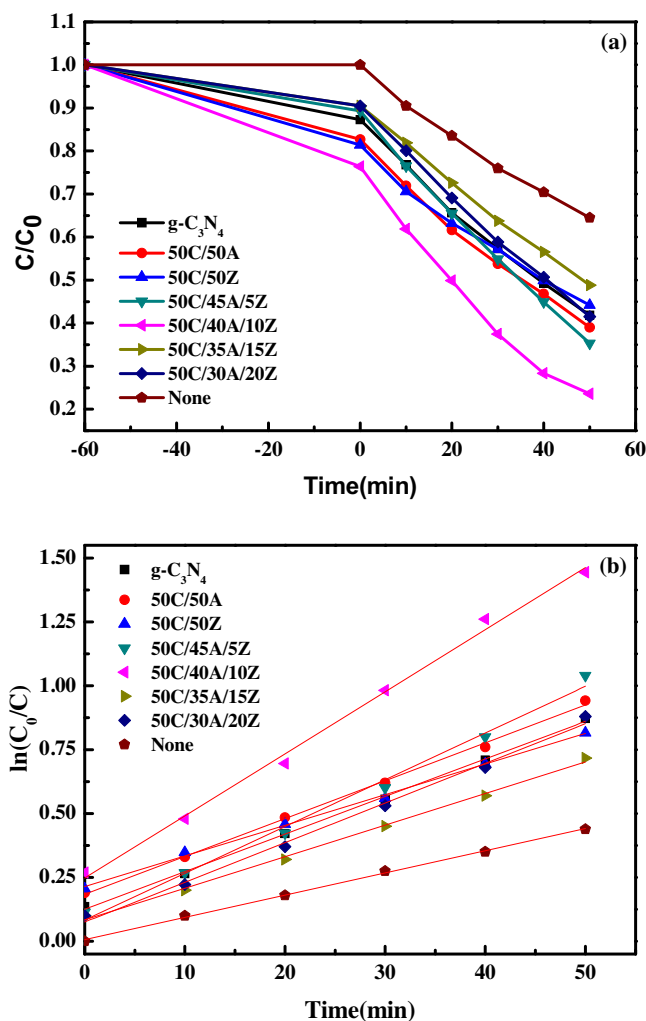


Fig. 6. Time-course variation of (a) C/C_0 and (b) $\ln(C_0/C)$ of MB.

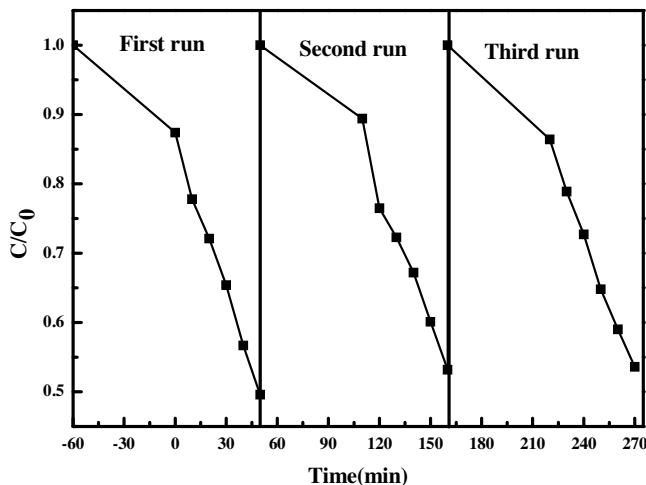


Fig. 7. Cycling runs in the photocatalytic degradation of MB over 50C/40A/10Z photocatalyst.

-1.13 V vs. SHE [17] and the band gap of $g\text{-C}_3\text{N}_4$ is 2.76 eV , meaning its potential of the highest occupied molecular orbital (HOMO) is 1.63 V , which is lower than the potentials of $\cdot\text{OH}/\text{H}_2\text{O}$ (2.27 V) [13] and $\cdot\text{OH}/\text{OH}^-$ (1.99 eV) [47]. Hence, the photo-induced holes on $g\text{-C}_3\text{N}_4$ could not oxidize H_2O or OH^- adsorbed on the surface

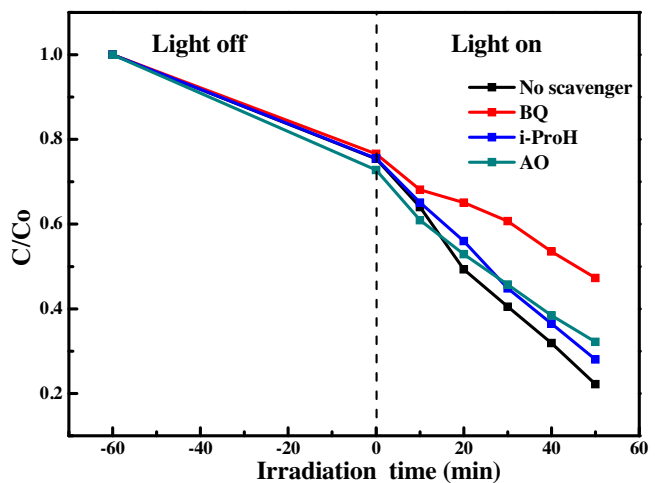


Fig. 8. Time-course variation of MB C/C_0 over 50C/40A/10Z in the presence of scavengers.

of photocatalyst to produce $\cdot\text{OH}$ radicals. It can be concluded that the $\cdot\text{OH}$ radicals are generated from the $\cdot\text{O}_2^-$ radicals, which are derived from the reaction between the O_2 and the photo-induced electrons on LUMO of $g\text{-C}_3\text{N}_4$.

To directly observe the generation of active oxygen species over various samples and compare their amount, the EPR signals of DMPO- $\cdot\text{O}_2^-$ and DMPO- $\cdot\text{OH}$ adducts are shown in Fig. 9. It can be seen from Fig. 9a that ternary 50C/40A/10Z heterojunction has the strongest signal, indicating its highest ability for producing $\cdot\text{O}_2^-$ radicals. At the same time, as shown in Fig. 9b, ternary heterojunction has the most intense peak for $\cdot\text{OH}$ radicals. The results confirm the superior molecular oxygen activation performance of ternary 50C/40A/10Z composite.

3.5. Characterization on carriers separation efficiency

Transient photocurrent is an effective method as a direct evidence to elucidate the separation efficiency of electron and hole [18]. As shown in Fig. 10, a towering and stable photocurrent response over all the samples is viewed for each on-off cycles. The ternary heterojunction shows the strongest photocurrent under visible light ($\lambda > 420\text{ nm}$) irradiation, which is 1.54 times higher than pure $g\text{-C}_3\text{N}_4$ and is in conformity with the rate of photocatalytic degradation of MB, indicating that the recombination of photo-induced e^-/h^+ is effectively restrained by employing Al_2O_3 to build a stair between $g\text{-C}_3\text{N}_4$ and ZnO .

The time-resolved fluorescence decay spectrum (Fig. 11) of $g\text{-C}_3\text{N}_4$ and ternary heterojunction is recorded to investigate the photophysical behavior of the photo-induced charge carriers. The fluorescent intensities of both materials decay exponentially. It is noteworthy that ternary heterojunction displays slow decay kinetics. The prolonged lifetime is generally related to the enhanced electron migration and/or electronic structure changes induced by the quantum confinement effect, which would also improve the probability of photo-induced carrier charges to be captured by O_2 or H^+ to exert redox roles [48]. In this case, $g\text{-C}_3\text{N}_4$ and ternary heterojunction exhibit three lives, which is consistent with the literature [49,50]. The shortest lifetime of 0.35 ns in the $g\text{-C}_3\text{N}_4$ increases to 0.41 ns in the ternary heterojunction. The medium lifetime of the charge carrier increases from 2.53 ns in $g\text{-C}_3\text{N}_4$ to 2.59 ns in ternary heterojunction. The longest lifetime of ternary heterojunction is up to 11.48 ns , about 1.48 ns longer than $g\text{-C}_3\text{N}_4$ (10.00 ns). It can be concluded from the prolonged lifetimes of charge carriers and the increased photocurrent of ternary heterojunction compared with those of pure $g\text{-C}_3\text{N}_4$ and binary heterojunctions that

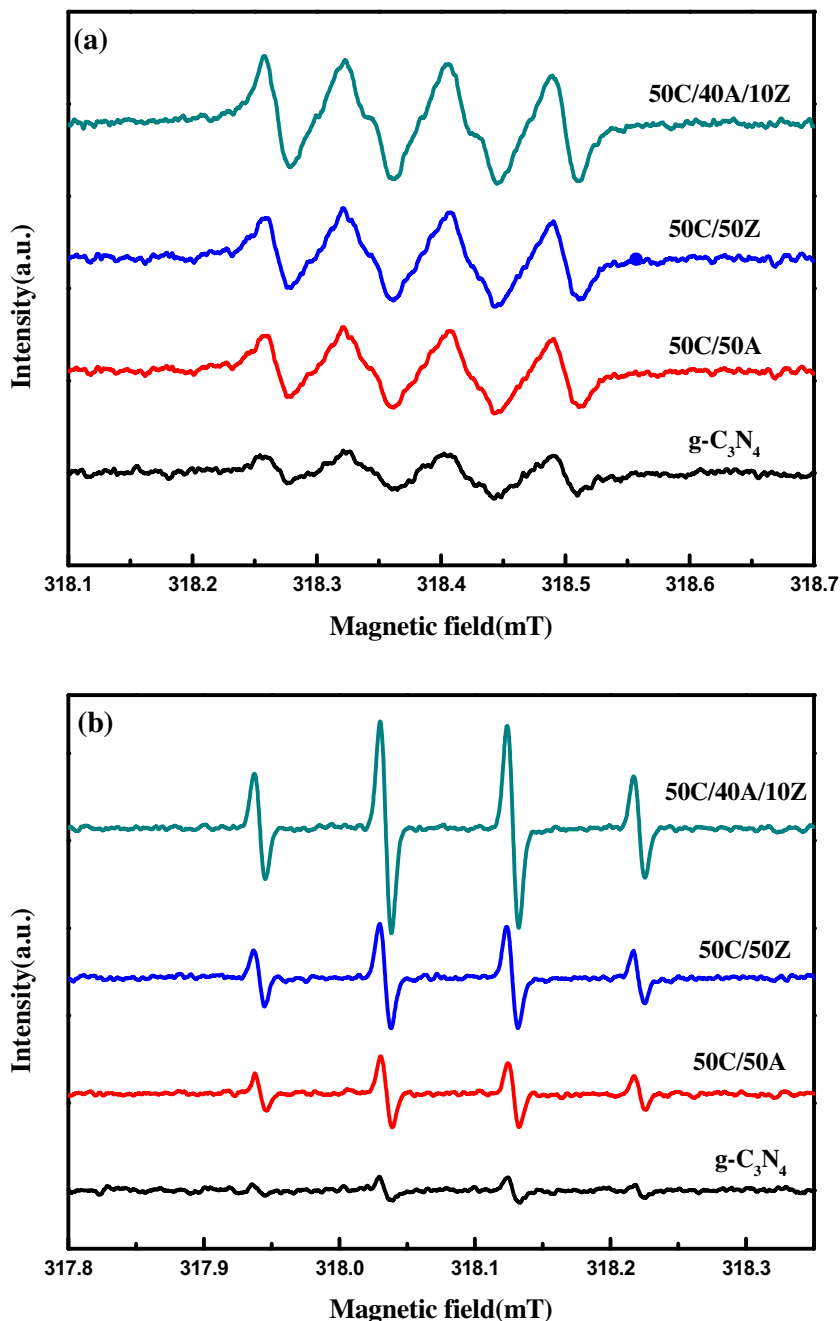


Fig. 9. (a) EPR signals of DMPO-•O₂⁻ adduct and (b) DMPO-•OH adduct over various photocatalysts after 12 min visible-light illumination.

the introduction of Al₂O₃ can effectively enhance the separation of photo-induced electrons and holes.

Fig. 12 shows electrochemical impedance spectra (EIS) Nyquist plots of pure g-C₃N₄, 50C/50Z and 50C/40A/10Z electrodes under visible light illumination. The arc radius on the EIS reflects the transfer rate on the interface of the electrode. The smaller arc radius means more effective separation of photo-induced electron-hole pairs and higher charge separation efficiency across the electrode-electrolyte interface. The arc radius of the ternary heterojunction electrode is the smallest among these samples, suggesting that amorphous Al₂O₃ can make the separation and transfer of photo-induced e⁻-h⁺ pairs more efficient, which is in good accordance with the result of our conjecture.

3.6. Energy band structure and cascade electron transfer route

To verify the feasibility of the charge separation over the ternary heterojunction, the energy band structure of each semiconductor should be investigated. **Fig. 13a** shows the UV-vis diffuse reflective spectra. It can be seen that the g-C₃N₄ has great absorbance in UV-vis light range of 200–500 nm, while ZnO and Al₂O₃ exhibit the ultraviolet light absorption almost in the wavelength < 400 nm. However, after introducing ZnO and/or Al₂O₃, there is nearly no change in absorbance for binary and ternary heterojunctions, even the content of g-C₃N₄ in the composites is only half of the pure g-C₃N₄. This phenomenon implies that synergistic effect between g-C₃N₄ and ZnO and/or Al₂O₃ is existed to enhance the photoabsorption performance [51], and the obtained materials are heterojunctions, instead of simple composites.

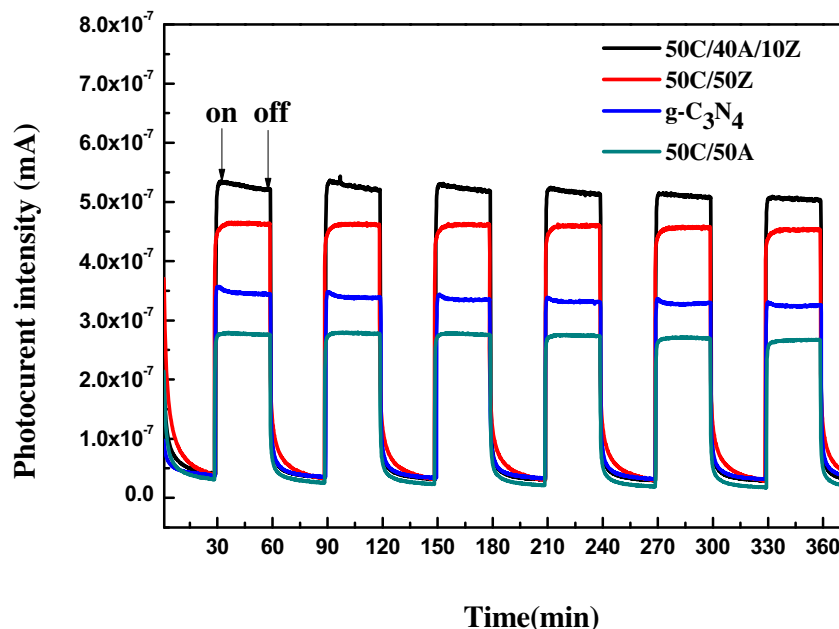


Fig. 10. Photocurrent of g-C₃N₄, 50C/50A, 50C/50Z, 50C/40A/10Z under visible light irradiation at a bias potential of zero vs Ag/AgCl in 0.2 M Na₂SO₄ aqueous solution.

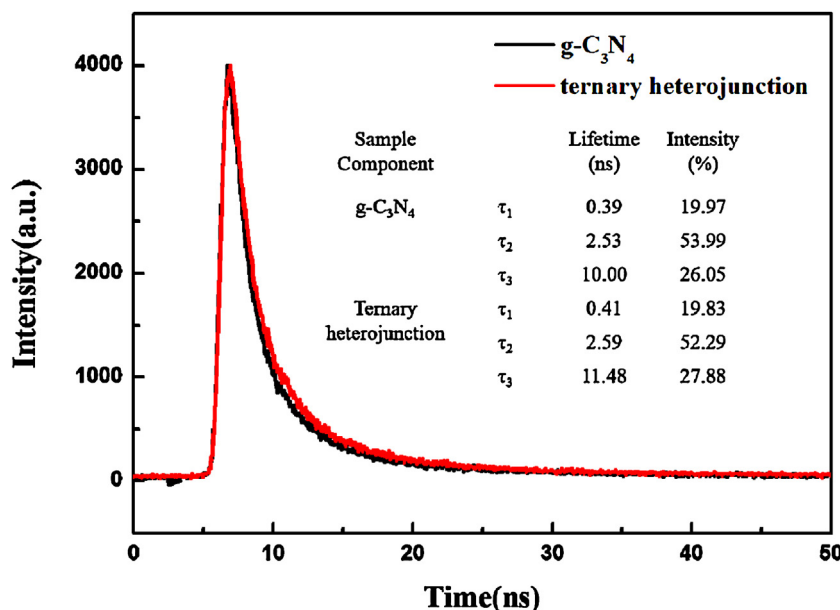


Fig. 11. PL decay curves measured at $\lambda_{\text{ex}} = 254$ nm and $\lambda_{\text{em}} = 550$ nm for g-C₃N₄ and 50C/40A/10Z ternary heterojunction.

The energy band-gap (E_g) can be estimated according to the expression of Tauc plots, $(\alpha h\nu)^n = K(h\nu - E_g)$ [52], where α represents the absorption coefficient, $h\nu$ is the photon energy, K is a constant, n is 2 for a direct transition and 1/2 for an indirect transition. The $(\alpha h\nu)^2$ vs. $h\nu$ curves for g-C₃N₄, ZnO and Al₂O₃, three direct transition semiconductors, are shown in Fig. 13b. The extrapolation of straight line to $(\alpha h\nu)^2 = 0$ axis can give the value of the band gap energy. The band gaps are estimated to be 2.76 eV, 3.20 eV, 4.86 eV for g-C₃N₄, ZnO and Al₂O₃, respectively.

Mott-Schottky (MS) measurements were conducted to obtain the conduction band (CB) positions of the photocatalysts. As illustrated in Fig. 14a, the Al₂O₃ and ZnO exhibit a positive slope, indicating their nature of n-type semiconductor. Meanwhile, the flat band potentials of Al₂O₃ and ZnO are -1.14 V and -0.89 V vs. Ag/AgCl, corresponding to -0.54 V and -0.29 V vs. reversible

hydrogen electrode (RHE), respectively, by using the relation of $E_{\text{RHE}} = E_{(\text{Ag}/\text{AgCl})} + 0.6 \text{ V}$ [53,54]. Furthermore, for n-type semiconductor, the flat band potential is believed to be close to the CB position [55]. Thus, the CB minimums of Al₂O₃ and ZnO should be at -0.54 and -0.29 V, respectively. Furthermore, the LUMO of g-C₃N₄ is thought to be at -1.13 V, thus the suitable energy gap structure provides theoretical basis for the free migration of photo-generated electron of g-C₃N₄ and the prolonging life of free electrons supplies the application prospect for g-C₃N₄/Al₂O₃/ZnO ternary heterojunctions in the aspect of oxygen activation because all their CB positions at the -1.13, -0.54, and -0.29 V of g-C₃N₄, Al₂O₃, and ZnO are more negative than -0.28 V, the redox potential of O₂/•O₂⁻ [13]. Combining their band gaps, the valence band (VB) positions are also calculated, as shown in Fig. 14b.

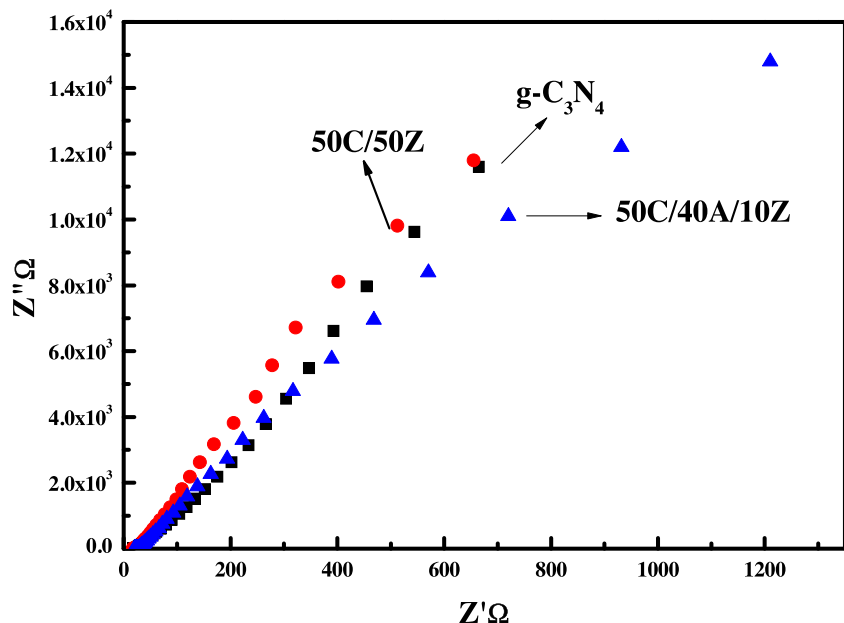
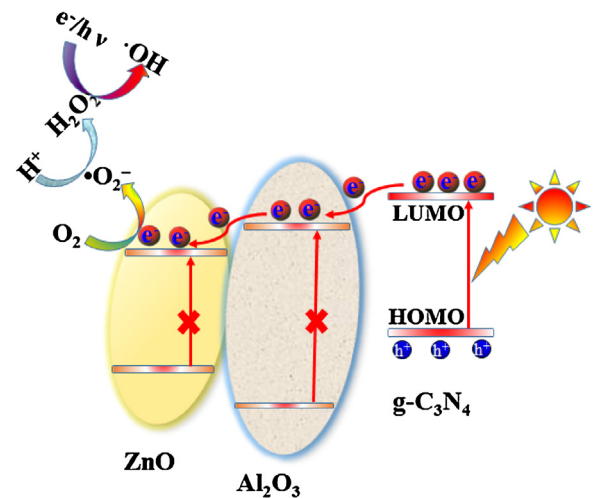
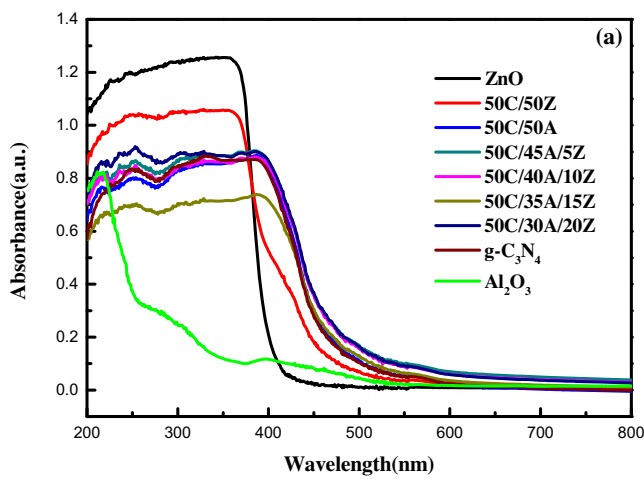


Fig. 12. Nyquist plots for pure g-C₃N₄, 50C/50Z and 50C/40A/10Z in aqueous solution under visible light (electrolyte: 0.2 M Na₂SO₄).



Scheme 3. Cascade electron transfer for O₂ activation over ternary g-C₃N₄/Al₂O₃/ZnO heterojunction under visible-light irradiation.

On the basis of the experimental results and material characterizations, a potential cascade electron transfer pathway over ternary g-C₃N₄/Al₂O₃/ZnO heterojunction under visible light is proposed as Scheme 3. Firstly, electrons in the HOMO of g-C₃N₄ are excited to the LUMO (-1.13 eV) upon visible-light illumination. Some of them would reduce O₂ adsorbed on the surface of g-C₃N₄ to generate •O₂⁻ radicals; some would migrate to the CB of defective Al₂O₃ and then flow to the CB of ZnO, forming the cascade transport route. The stepwise transfer are beneficial to the separation of photo-induced electrons and holes and the improvement of quantum efficiency. Secondly, the electrons on Al₂O₃ or ZnO could capture and activate molecular oxygen to produce •O₂⁻ and •OH. Thirdly, the left photogenerated holes on the HOMO of g-C₃N₄ can participate in the oxidation reaction.

4. Conclusions

In summary, ternary g-C₃N₄/Al₂O₃/ZnO heterojunctions have been successfully synthesized via a green co-precipitation and the

Fig. 13. (a) UV-vis DRS spectra for as-prepared Al₂O₃, g-C₃N₄, binary and ternary heterojunctions, and (b) $(\alpha h\nu)^2$ versus $h\nu$ curves for g-C₃N₄, ZnO, and Al₂O₃.

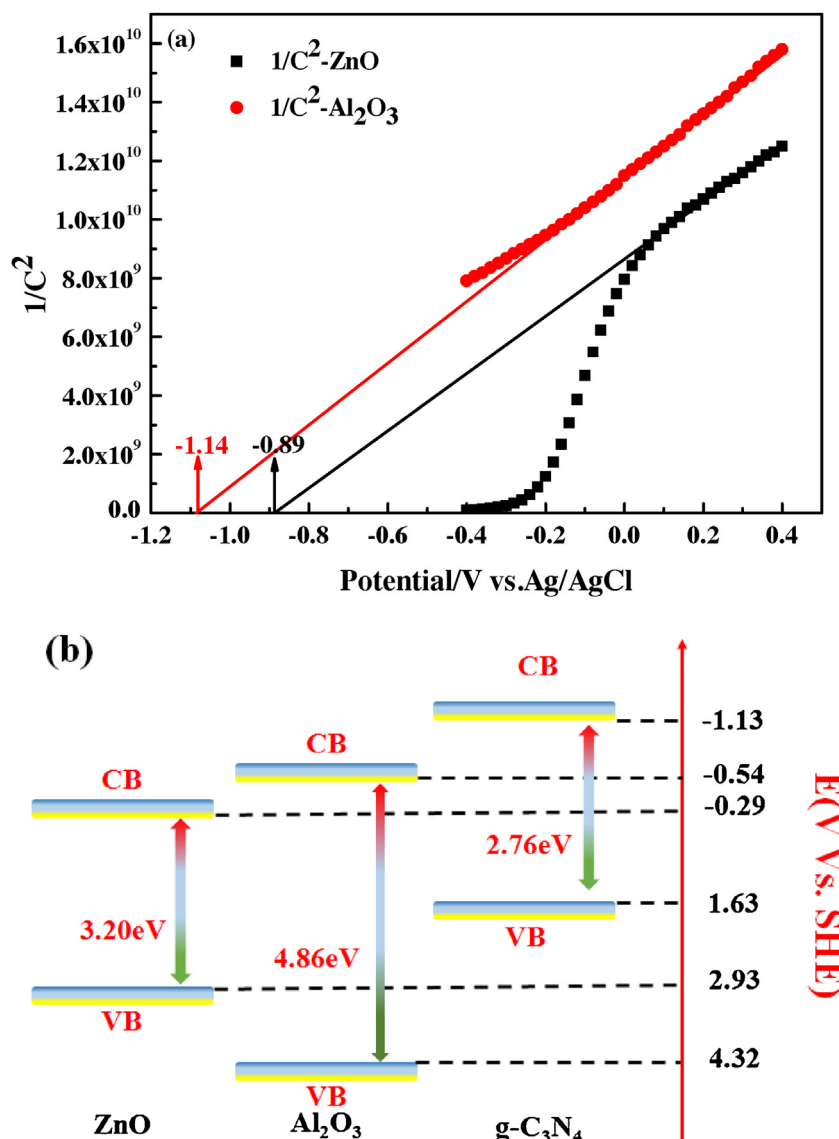


Fig. 14. (a) Mott–Schottky plots of the Al_2O_3 and ZnO electrodes in 0.2 M Na_2SO_4 aqueous solution under visible light with an amplitude of 5 mV at each potential, (b) energy band positions of ZnO , Al_2O_3 and $\text{g-C}_3\text{N}_4$.

following calcination. The amorphous Al_2O_3 acts as mediated material for matching the lattice of $\text{g-C}_3\text{N}_4$ and ZnO because of its disordered atomic arrangement, which could enhance the electron transfer probability. Meanwhile, the conduction band potential of defective Al_2O_3 obtained via precipitation is measured at -0.54 V for the first time, which is in the middle of those of $\text{g-C}_3\text{N}_4$ and ZnO . Thus, ternary $\text{g-C}_3\text{N}_4/\text{Al}_2\text{O}_3/\text{ZnO}$ heterojunction exhibits cascade electron transfer route and superior molecular oxygen activation performance. The heterojunction containing 50% $\text{g-C}_3\text{N}_4$, 40% Al_2O_3 , and 10% ZnO (weight ratio) shows the highest oxygen activation ability and photocatalytic activity.

Acknowledgements

We are grateful for the financial support from the National Natural Science Foundation of China (21376061), the Natural Science Foundation for Distinguished Young Scholars of Hebei Province (B2015208010), the Scientific Research Foundation for High-Level Talent in University of Hebei Province (GCC2014057), and Foundation for the Returned Overseas Chinese Scholars of Hebei Province (CL201609).

References

- [1] M. Metz, E.I. Solomon, J. Am. Chem. Soc. 123 (2001) 4938–4950.
- [2] X.L. Jin, L.Q. Ye, H. Wang, Y.R. Su, H.Q. Xie, Z.G. Zhong, H. Zhang, Appl. Catal. B 165 (2015) 668–675.
- [3] W.W. He, H.K. Kim, W.G. Wamer, D. Melka, J.H. Callahan, J.J. Yin, J. Am. Chem. Soc. 136 (2014) 750–757.
- [4] S.S. Gill, N. Tuteja, Plant Physiol. Biochem. 48 (2010) 909–930.
- [5] C.R. Chang, Z.Q. Huang, J. Li, Nano Res. 8 (2015) 3737–3748.
- [6] D. Widmann, R.J. Behm, Acc. Chem. Res. 47 (2014) 740–749.
- [7] C.S. Hinde, D. Ansovini, P.P. Wells, G. Collins, S.V. Aswegen, J.D. Holmes, T.S.A. Hor, R. Raja, ACS Catal. 6 (2015) 3807–3816.
- [8] Y. Shiraishi, S. Kanazawa, Y. Sugano, D. Tsukamoto, H. Sakamoto, S. Ichikawa, T. Hirai, ACS Catal. 4 (2014) 774–780.
- [9] H. Li, J.G. Shi, K. Zhao, L.Z. Zhang, Nanoscale 6 (2014) 14168–14173.
- [10] J. Di, J.X. Xia, M.X. Ji, B. Wang, S. Yin, Y. Huang, Z.G. Chen, H.M. Li, Appl. Catal. B 188 (2016) 376–387.
- [11] X.M. Shen, W.Q. Liu, X.J. Gao, Z.H. Lu, X.C. Wu, X.F. Gao, J. Am. Chem. Soc. 137 (2015) 15882–15891.
- [12] H. Zhang, L.H. Guo, L.X. Zhao, B. Wan, Y. Yang, J. Phys. Chem. Lett. 6 (2015) 958–963.
- [13] A. Fujishima, X.T. Zhang, C.R. Chim. 9 (2006) 750–760.
- [14] G.G. Zhang, G.A. Lan, X.C. Wang, Angew. Chem. Int. Ed. 55 (2016) 15712–15727.
- [15] W.J. Ong, L.L. Tan, Y.H. Ng, S.T. Yong, S.P. Chai, Chem. Rev. 116 (2016) 7159–7329.

- [16] X.C. Wang, K. Maeda, A. Thomas, K. Takanabe, G. Xin, J.M. Carlsson, K. Domen, M. Antonietti, *Nat. Mater.* 8 (2009) 76–80.
- [17] D.S. Wang, H.T. Sun, Q.Z. Luo, X.L. Yang, R. Yin, *Appl. Catal. B* 156 (2014) 323–330.
- [18] F.T. Li, S.J. Liu, Y.B. Xue, X.J. Wang, Y.J. Hao, J. Zhao, R.H. Liu, D.S. Zhao, *Chem. Eur. J.* 21 (2015) 10149–10159.
- [19] G.G. Zhang, Z.A. Lan, L.H. Lin, S. Lin, X.C. Wang, *Chem. Sci.* 7 (2016) 3062–3066.
- [20] T. Sano, K. Koike, T. Hori, T. Hirakawa, Y. Ohko, K. Takeuchi, *Appl. Catal. B: Environ.* 198 (2016) 133–141.
- [21] Z.A. Lan, G.G. Zhang, X.C. Wang, *Appl. Catal. B: Environ.* 192 (2016) 116–125.
- [22] Z.S. Zhang, M. Wang, W.Q. Cui, H. Sui, *RSC Adv.* 7 (2017) 8167–8177.
- [23] L. Liu, Y.H. Qi, J.Y. Yang, W.Q. Cui, X.G. Li, Z.S. Li, *Appl. Sur. Sci.* 358 (2015) 319–327.
- [24] T.T. Yu, L.F. Liu, L. Li, F.L. Yang, *Electrochim. Acta* 210 (2016) 122–129.
- [25] C.S. Pan, J. Xu, Y.J. Wang, D. Li, Y.F. Zhu, *Adv. Funct. Mater.* 22 (2012) 1518–1524.
- [26] D.M. Chen, K.W. Wang, D.G. Xiang, R.L. Zong, W.Q. Yao, Y.F. Zhu, *Appl. Catal. B* 147 (2014) 554–561.
- [27] C. Liu, C.M. Li, X.D. Fu, F. Raziq, Y. Qu, L.Q. Jing, *RSC Adv.* 5 (2015) 37275–37280.
- [28] F.T. Li, Y. Zhao, Q. Wang, X.J. Wang, Y.J. Hao, R.H. Liu, D.S. Zhao, *J. Hazard. Mater.* 283 (2015) 371–381.
- [29] F.T. Li, Y.B. Xue, B. Li, Y.J. Hao, X.J. Wang, R.H. Liu, D.S. Zhao, *Ind. Eng. Chem. Res.* 53 (2014) 19540–19549.
- [30] X.J. Wang, C. Liu, X.L. Li, F.T. Li, Y.P. Li, J. Zhao, R.H. Liu, *Appl. Sur. Sci.* 394 (2017) 340–350.
- [31] B.H.J. Bielski, G.G. Shiue, S. Bajuk, *J. Phys. Chem.* 84 (1980) 830–833.
- [32] M. Quinones, Y. Zhang, P. Riascos, H.M. Hwang, W.G. Aker, X. He, R.M. Gao, *Photochem. Photobiol.* 90 (2014) 374–379.
- [33] K.I. Ishibashi, A. Fujishima, T. Watanabe, K. Hashimoto, *Electrochem. Commun.* 2 (2000) 207–210.
- [34] X.J. Bai, L. Wang, Y.J. Wang, W.Q. Yao, Y.F. Zhu, *Appl. Catal. B* 152–153 (2014) 262–270.
- [35] D. Ghosh, G. Periyasamy, S.K. Pati, *J. Phys. Chem. C* 118 (2014) 15487–15494.
- [36] H.G. Yu, R. Liu, X.F. Wang, P. Wang, J.G. Yu, *Appl. Catal. B: Environ.* 111–112 (2012) 326–333.
- [37] C.D. Wagner, D.E. Passoja, H.F. Hillery, T.G. Kinisky, H.A. Six, W.T. Jansen, J.A. Taylor, *J. Vac. Sci. Technol.* 21 (1982) 933–944.
- [38] L.P.H. Jeurgens, W.G. Sloof, F.D. Tichelaar, E.J. Mittemeijera, *Surf. Sci.* 506 (2002) 313–332.
- [39] D.H. Xu, D.H. Fan, W.Z. Shen, *Nanoscale Res. Lett.* 8 (2013) 1–9.
- [40] W.C. Wan, S. Yu, F. Dong, Q. Zhang, Y. Zhou, *J. Mater. Chem. A* 4 (2016) 7823–7829.
- [41] W.J. Li, D.Z. Li, Y.M. Lin, P.X. Wang, W. Chen, X.Z. Fu, Y. Shao, *J. Phys. Chem. C* 116 (2012) 3552–3560.
- [42] F.T. Li, Y. Zhao, Y. Liu, Y.J. Hao, R.H. Liu, D.S. Zhao, *Chem. Eng. J.* 173 (2011) 750–759.
- [43] F.T. Li, Y. Zhao, Q. Wang, X.J. Wang, Y.J. Hao, R.H. Liu, D.S. Zhao, *J. Hazard. Mater.* 239 (2012) 118–127.
- [44] S.X. Ge, L.Z. Zhang, *Environ. Sci. Technol.* 45 (2011) 3027–3033.
- [45] J.H. Kou, Z.S. Li, Y.P. Yuan, H.T. Zhang, Y. Wang, Z.G. Zou, *Environ. Sci. Technol.* 43 (2009) 2919–2924.
- [46] Y.X. Chen, S.Y. Yang, K. Wang, L.P. Lou, *J. Photoch. Photobio. A* 172 (2005) 47–54.
- [47] S. Kim, W. Choi, *Environ. Sci. Technol.* 36 (2002) 2019–2025.
- [48] L.T. Ma, H.Q. Fan, M.M. Li, H.L. Tian, J.W. Fang, G.Z. Dong, *J. Mater. Chem. A* 3 (2015) 22404–22412.
- [49] J. Chen, S.H. Shen, P. Wu, L.J. Guo, *Green Chem.* 17 (2015) 509–517.
- [50] Y.L. Chen, J.H. Li, Z.H. Hong, B. Shen, B.Z. Lin, B.F. Gao, *Phys. Chem. Chem. Phys.* 16 (2014) 8106–8113.
- [51] K. Dai, L.H. Lu, C.H. Liang, Q. Liu, G.P. Zhu, *Appl. Catal. B* 156–157 (2014) 331–340.
- [52] J. Tauc (Ed.), *Amorphous and Liquid Semiconductors*, Plenum Press, New York, 1974.
- [53] S.J. Hong, S. Lee, J.S. Jang, J.S. Lee, *Energy Environ. Sci.* 4 (2011) 1781–1787.
- [54] F.T. Li, Y.L. Li, M.J. Chai, B. Li, Y.J. Hao, X.J. Wang, R.H. Liu, *Catal. Sci. Technol.* 6 (2016) 7895–7995.
- [55] M. Zhang, X.J. Bai, D. Liu, J. Wang, Y.F. Zhu, *Appl. Catal. B* 164 (2015) 77–81.